Reprinted from JOURNAL OF COMPUTATIONAL PHYSICS
All Rights Reserved by Academic Press, New York and London

Vol. 89, No. 2, August 1990
Printed in Belgium

Solving Time-Dependent Two-Dimensional Eddy Current Problems

MIN EIG LEE,[†] S. I. HARIHARAN,[*,‡] AND NATHAN IDA[†]

[*]*Department of Mathematical Sciences, and*
[†]*Department of Electrical Engineering,*
The University of Akron, Akron, Ohio 44325-4002

Received April 29, 1988; revised May 23, 1989

In this paper we report our results on transient eddy current calculations. A typical situation describes a two-dimensional transverse magnetic field incident on an infinitely long conductor. The conductor is assumed to be a good conductor but not a perfect one. Electromagnetic wave scattering and field penetration occur in this situation. The resulting problem is an initial boundary-value interface problem with the boundary of the conductor being the interface. A potential function is defined to model the situation in the time domain. Finite-difference time-domain (FD-TD) techniques are used to march the potential function explicitly in time. Treatment of low-frequency radiation condition is given special consideration. Results are validated with approximate analytic solutions. © 1990 Academic Press, Inc.

1. INTRODUCTION

Eddy current calculation is an important subject in classical electrodynamics. Eddy currents are induced in a conductor, when an electromagnetic field is incident upon it. Therefore, the phenomena of wave propagation, scattering, and penetration are integrated in eddy current problems. Usually these result in flows of currents in a region near the boundary. A common way of treating these problems, in particular, the induced currents, relies on estimating an appropriate skin depth for the conductor. Once the skin depth is determined, the associated fields are obtained through an equivalence principle by imposing a boundary condition on the region of current formulation. Estimation of the skin depth, as given in a later section, is based on the field penetration into an infinite planar slab. In high-frequency situations, the skin depths are very small. Compared to the skin depth, the boundary of the conductor can be reasonably approximated by an infinite plane. In low-frequency cases, if the conductor is small and happens to have a geometry other than that of a planar slab, the procedure mentioned above will not work well. Moreover, the incident waves need not be restricted to time-harmonic waves, in general. Pulse sources and surge waves which come from thunder or

[‡] Work was supported by the National Science Foundation Grant DMS-8604047, and in part by NASA while the author was visiting ICOMP, NASA Lewis Research Center. Use of the Ohio Supercomputer Center's Cray X-MP computer is also acknowledged.

0021-9991/90 $3.00

circuit breakers arise in practice. Therefore, one must have a procedure which can capture the transient behavior of eddy currents.

Along this line, an effort was begun in [1], where a two-dimensional eddy current problem was considered in the frequency domain. The boundary integral equation procedures were established in this work. It presented some possibilities for further improvements and the feasibility of solving this class of problems in three dimensions. The work in [2] dealt with the continuation of [1] in conjunction with the finite element methods. Unfortunately, only the theoretical details were available. Moreover, the treatment for a three-dimensional problem was restricted to the time-harmonic field. It was established in [3, 4] that the finite difference methods are effective even for the frequency-domain problems. Our goal is to use the finite difference methods to solve these problems, in particular, the two-dimensional problems, in the time domain.

The finite-difference time-domain (FD-TD) techniques were first applied, in 1966 [5], to solve the two-dimensional electromagnetic scattering problems. In this work, the time-marching methods for solving Maxwell's equations were proposed. Since then, a large amount of work has been done for the problems associated with Maxwell's equations in the time domain. An example was given in [6], which concentrated on the penetration through an aperture into complex geometries. As mentioned, electromagnetic penetration problems were difficult to solve through many analytical and numerical methods. The main difficulty of the FD-TD lied in obtaining the appropriate absorbing boundary conditions exterior to the obstacle. Without these conditions, there would be considerable nonphysical reflections coming from the boundary into the domain of interest. In [7–9], many efforts were made to overcome this difficulty. Following the idea of [10], [7] proposed the second-order boundary conditions for the vector-field codes. References [8, 9] applied these conditions to obtain the highly accurate near and far field results for both 2D and 3D targets, even with the grid truncations pushed as close as 10 space cells away from the target. However, the boundary conditions in [7] used the high-frequency approximations. These are not applicable here, since the eddy current calculations are inherently the low-frequency problems. In this paper, we present our approach to overcome this difficulty.

Most of the previous work, in the area of electromagnetic wave radiation and scattering, concentrated on using the vector-field codes. In general, four first-order Maxwell's equations must be solved. However, by defining potential functions in terms of the field vectors, it is possible to transform the four first-order field equations into two second-order potential equations [11]. For the two-dimensional problem we consider here, only one potential function is needed. Thus, with the time-stepping of potentials, the requirement for computer storage can be lowered and the procedures of calculation can be simplified. In this paper we report the feasibility of this idea. Since the paper deals with potentials, the uniqueness of the solution is important. We prove this for our numerical model in Appendix A.

Compared to literature, the results we report here have the following distinctive features:

1. A low-frequency radiation boundary condition (RBC).
2. Time-stepping of potentials rather than vector field components.
3. An application to very low frequency wave penetrating into conducting structures.

2. Formulation of the Problem

Let Ω be the cross-section region, in the x-y plane, of a conducting cylinder with a finite conductivity σ_m, a permeability μ_m, and a permittivity ε_m. The generators of the cylinder are parallel to the z-axis. The ambient medium is the air with a permeability μ_a and a permittivity ε_a. The conductivity of the air is neglected because it does not play a major role in this type of calculations. If desired, it could be incorporated into the model, in which case the procedure we discuss

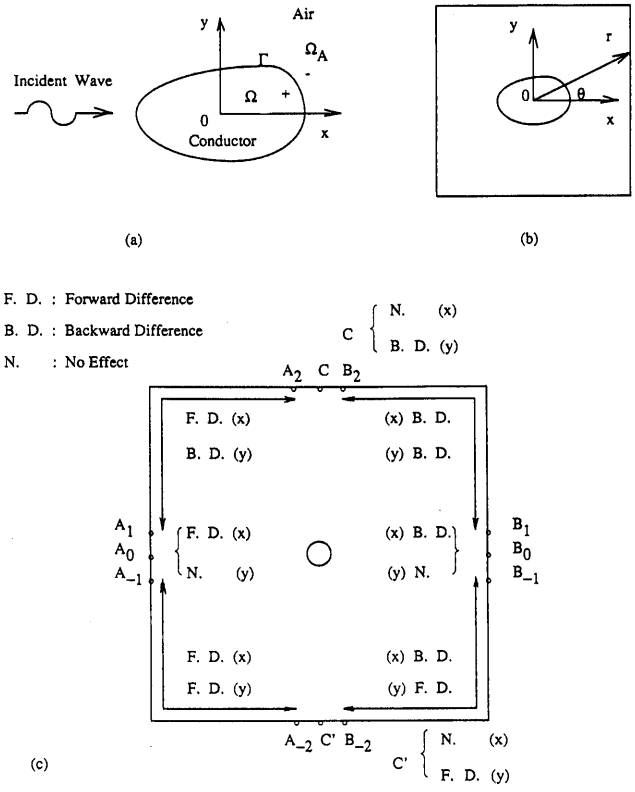

FIG. 1. (a) Typical situation of the problem. (b) Coordinates of the computational domain. (c) Implementation of the radiation condition.

would still be valid. The incident field has the form: $\mathbf{E}_i = E_i(x, y, t)\mathbf{k}$, and $\mathbf{H}_i = H_{i1}(x, y, t)\mathbf{i} + H_{i2}(x, y, t)\mathbf{j}$. A typical situation is depicted in Fig. 1(a). The electric field is parallel to the axis of the cylinder. The magnetic field is transverse (TM) and is in the x-y plane. For simplicity, we assume that all material properties are homogeneous, isotropic, and frequency-independent. Writing Maxwell's equations, one obtains two sets of equations that are valid outside and inside the conductor, respectively.

In Ω_A (air)

$$\frac{\partial H_1}{\partial x} + \frac{\partial H_2}{\partial y} = 0, \tag{1}$$

$$\frac{\partial E}{\partial y}\mathbf{i} - \frac{\partial E}{\partial x}\mathbf{j} = -\mu_a\left(\frac{\partial H_1}{\partial t}\mathbf{i} + \frac{\partial H_2}{\partial t}\mathbf{j}\right), \tag{2}$$

$$\frac{\partial H_2}{\partial x} - \frac{\partial H_1}{\partial y} = \varepsilon_a \frac{\partial E}{\partial t}. \tag{3}$$

In Ω (conductor)

$$\frac{\partial H_1}{\partial x} + \frac{\partial H_2}{\partial y} = 0, \tag{4}$$

$$\frac{\partial E}{\partial y}\mathbf{i} - \frac{\partial E}{\partial x}\mathbf{j} = -\mu_m\left(\frac{\partial H_1}{\partial t}\mathbf{i} + \frac{\partial H_2}{\partial t}\mathbf{j}\right), \tag{5}$$

$$\frac{\partial H_2}{\partial x} - \frac{\partial H_1}{\partial y} = \sigma_m E + \varepsilon_m \frac{\partial E}{\partial t}. \tag{6}$$

The first term on the right side of (6) is the conduction current. The second term is the displacement current. In addition, the following conditions are needed to make the problem well-posed. On Γ (boundary of Ω), the tangential components of $\mathbf{E}$ and $\mathbf{H}$ are continuous, i.e., no surface current density is assumed. At infinity, the scattered $\mathbf{E}$ and $\mathbf{H}$ both decay to zero (radiation condition).

The zero divergence and two-dimensionality of $\mathbf{H}$ in both regions suggest the existence of a scalar function Ψ such that $H_1 = \partial\Psi/\partial y$ and $H_2 = -\partial\Psi/\partial x$. Substituting these in Eq. (2) and (5), we see that $E = -\mu\,\partial\Psi/\partial t$. The function $\mu\Psi\mathbf{k}$ is identified as the magnetic vector potential. In turn, using this scalar function, the dimensionless problem can be written as follows: Details of the derivation of the dimensionless form are available in [12]. The governing equations are

$$\frac{\partial^2\Psi}{\partial x^2} + \frac{\partial^2\Psi}{\partial y^2} = \omega^2 L^2 \mu_a \varepsilon_a \frac{\partial^2\Psi}{\partial t^2} \qquad \text{in } \Omega_A, \tag{7}$$

$$\frac{\partial^2\Psi}{\partial x^2} + \frac{\partial^2\Psi}{\partial y^2} = \omega L^2 \mu_m \sigma_m \frac{\partial\Psi}{\partial t} + \omega^2 L^2 \mu_m \varepsilon_m \frac{\partial^2\Psi}{\partial t^2} \qquad \text{in } \Omega, \tag{8}$$

where ω is the angular velocity of the incident wave and L is a length for scaling, which is on the order of the scatterer's radius. The interface conditions (on Γ) are $\Psi^- = \mu_r \Psi^+$ and $\partial\Psi^-/\partial n = \partial\Psi^+/\partial n$, where the minus sign represents the exterior field, the plus sign represents the interior field, and μ_r is the relative permeability of the conductor. The initial conditions are $\Psi(x, y, 0) = \Psi_{\text{inc}}(x, y, 0)$ and $\partial\Psi(x, y, 0)/\partial t = \partial\Psi_{\text{inc}}(x, y, 0)/\partial t$, where Ψ_{inc} represents the incident wave. Sommerfeld's radiation condition is

$$\lim_{r\to\infty} r^{1/2}\left(\frac{\partial\Psi_s}{\partial r} + k_a \frac{\partial\Psi_s}{\partial t}\right) = 0, \tag{9}$$

where Ψ_s represents the scattered wave, $k_a = \omega L\sqrt{\mu_a \varepsilon_a}$, and r is the distance from the radiation boundary to the scattering center.

The model presented above is an interface problem with Γ being the interface. This model is also applicable to the calculation of wave scattering by lossy dielectrics and the nondestructive evaluation (NDE) of various kinds of composite materials. In the NDE of composite materials, μ_m and ε_m are no longer constants. Rather, they are functions of space. The frequency of the incident wave may range from low to microwave frequency. In this paper, the low-frequency eddy current problem is considered. The difficulties of the problem are explained as follows. For instance, if we consider a 60 Hz incident field and a conductor with a diameter of 0.3141593 m, the parameters that appear in Eq. (7) and (8) have the values: $k_a = \omega L\sqrt{\mu_a \varepsilon_a} = 2.514987 \times 10^{-7}$, $k'_m = \omega L\sqrt{\mu_m \varepsilon_m} = 2.514987 \times 10^{-7}$, $l'_m = L\sqrt{\omega \mu_m \sigma_m} = 26.55045$. Here we have used: $\mu_a = \mu_m = 1.256637 \times 10^{-6}$, $\varepsilon_a = \varepsilon_m = 8.854 \times 10^{-12}$, $\sigma_m = 3.72 \times 10^7$, and $L = 0.2$ in the MKS unit system. Thus, reconsidering Eq. (7), we see that it behaves like Laplace's equation, while Eq. (8) behaves like a parabolic equation. These observations were made in [13]. This only yields an approximation to the model given in Eq. (7) and (8). We believe that even though the value of k_a is extremely small, the problem is still governed by a wave phenomenon. This is further justified by the results we present later. Thus, we do not approximate the physical model, but rather present the procedures to solve the problem. This yields several difficulties, particularly in terms of computation. Our treatment is presented in the coming sections.

Retaining the wave nature in the exterior region, we further scale the problem for the purpose of treating boundary conditions. We scale the time by k_a. As a result, the governing equations take the form

$$\frac{\partial^2\Psi}{\partial x^2} + \frac{\partial^2\Psi}{\partial y^2} = \frac{\partial^2\Psi}{\partial t^2} \qquad \text{in } \Omega_A, \tag{10}$$

$$\frac{\partial^2\Psi}{\partial x^2} + \frac{\partial^2\Psi}{\partial y^2} = l_m^2 \frac{\partial\Psi}{\partial t} + k_m^2 \frac{\partial^2\Psi}{\partial t^2} \qquad \text{in } \Omega, \tag{11}$$

where

$$l_m^2 = \frac{\omega L^2 \mu_m \sigma_m}{k_a} \quad \text{and} \quad k_m^2 = \frac{\omega^2 L^2 \mu_m \varepsilon_m}{k_a^2}.$$

The radiation condition takes the form

$$\lim_{r \to \infty} r^{1/2} \left(\frac{\partial \Psi_s}{\partial r} + \frac{\partial \Psi_s}{\partial t} \right) = 0. \tag{12}$$

The interface conditions and the initial conditions remain the same.

3. Radiation Condition

The radiation condition (12) is difficult to implement numerically. It must be approximated in a suitable way before it is imposed on an artificial boundary. For the waves with moderate to high frequencies, the radiation boundary conditions are well known. The procedure is to write the far-field scattered wave in the form:

$$\Psi_s = \frac{f(k_a(r-t))}{\sqrt{r}} \left(a_0(\theta) + \frac{a_1(\theta)}{r} + \frac{a_2(\theta)}{r^2} + \cdots \right). \tag{13}$$

This expression follows from [14]. From this, it is easily verified that Ψ_s satisfies

$$\frac{\partial \Psi_s}{\partial r} + \frac{\partial \Psi_s}{\partial t} + \frac{1}{2r} \Psi_s = O\left(\frac{1}{r^{5/2}} \right). \tag{14}$$

This is the first-order radiation condition proposed in [10]. Moreover, in [15] the authors obtained a family of radiation conditions following the ideas of [14, 16]. The first-order radiation conditions of [15, 10] are the same. Their higher-order conditions differ from each other. The radiation boundary of (14) must be at least one wavelength away from the scattering center. This is suitable for the problems involving high-frequency waves. However, for low-frequency waves, Eq. (14) does not provide satisfactory solutions in a reasonable computational domain. This is due to the fact that the wavelengths are much longer than the size of the scatterer. This makes (14) impractical for the numerical implementation in low-frequency cases. Thus, we present an alternate formulation for the low-frequency situations.

3.1. *Approximation for Scattered Waves*

The wave equation in the exterior region is: $\nabla^2 \Psi = \partial^2 \Psi / \partial t^2$, where ∇^2 is the Laplacian operator. An incident wave, which propagates in the x direction, has the following form: $\Psi_i = f(k_a(x-t))$. As suggested in [13], the low-frequency wave

equations behave close to Laplace's equation. The solution of Laplace's equation has the following form:

$$u = \alpha + \beta \ln r + \sum_{i=1}^{\infty} \frac{\alpha_n(\theta)}{r^n}. \tag{15}$$

Since Laplace's equation has no characteristics of wave propagation, this approximation explains only the field distribution in space. To include the wave phenomena, we suggest that a term is incorporated to express the scattered waves as follows:

$$\Psi_s = \left[\alpha + \beta \ln r + \sum_{i=1}^{\infty} \frac{\alpha_n(\theta)}{r^n}\right] f(k_a(r-t)). \tag{16}$$

Neglecting the variation in the θ direction, the scattered waves must satisfy the following equation:

$$\frac{1}{r}\frac{\partial}{\partial r}\left(r\frac{\partial \Psi_s}{\partial r}\right) = \frac{\partial^2 \Psi_s}{\partial t^2}. \tag{17}$$

If the first two terms in (16) are used for Ψ_s, i.e., $\Psi_s = (\alpha + \beta \ln r) f(k_a(r-t))$, we obtain

$$\frac{1}{r}\frac{\partial}{\partial r}\left(r\frac{\partial \Psi_s}{\partial r}\right) - \frac{\partial^2 \Psi_s}{\partial t^2} = \frac{k_a(\alpha + 2\beta + \beta \ln r)}{r} f'[k_a(r-t)]. \tag{18}$$

For low frequency waves, $k_a \approx 0$. $f'[k_a(r-t)]$ is usually not too large. In the exterior region, the right-hand side of (18) is approximately 0. Therefore, on a boundary where the θ dependence is negligible, $\Psi_s = (\alpha + \beta \ln r) f(k_a(r-t))$ is an approximate solution for the scattered waves, with an accuracy on the order of k_a.

3.2. *Derivation of Boundary Condition*

From (16), Ψ_s is written in the following form:

$$\Psi_s = \left[\alpha + \beta \ln r + \frac{\alpha_1(\theta)}{r}\right] f(k_a(r-t)) + O\left(\frac{1}{r^2}\right). \tag{19}$$

Taking derivatives, we have

$$\frac{\partial \Psi_s}{\partial r} = \left[\frac{\beta}{r} - \frac{\alpha_1(\theta)}{r^2}\right] f(k_a(r-t)) + \left[\alpha + \beta \ln r + \frac{\alpha_1(\theta)}{r}\right] k_a f'(k_a(r-t)) + O\left(\frac{1}{r^2}\right), \tag{20}$$

$$\frac{\partial \Psi_s}{\partial t} = -\left[\alpha + \beta \ln r + \frac{\alpha_1(\theta)}{r}\right] k_a f'[k_a(r-t)] + O\left(\frac{1}{r^2}\right). \tag{21}$$

When both derivatives are added together,

$$\frac{\partial \Psi_s}{\partial r}+\frac{\partial \Psi_s}{\partial t}=\frac{\beta}{r}f(k_a(r-t))+O\left(\frac{1}{r^2}\right). \tag{22}$$

$f(k_a(r-t))$ is related to Ψ_s in the following way:

$$f(k_a(r-t))=\frac{1}{\alpha+\beta \ln r}\left[\Psi_s-\sum_{n=1}^{\infty}\frac{\alpha_n(\theta)}{r^n}f(k_a(r-t))\right]. \tag{23}$$

Substituting (23) into (22), we have

$$\frac{\partial \Psi_s}{\partial r}+\frac{\partial \Psi_s}{\partial t}=\frac{\beta}{r(\alpha+\beta \ln r)}\Psi_s+O\left(\frac{1}{r^2}\right). \tag{24}$$

Therefore, the low-frequency radiation boundary condition is obtained as

$$\frac{\partial \Psi_s}{\partial r}+\frac{\partial \Psi_s}{\partial t}+A(r)\Psi_s=O\left(\frac{1}{r^2}\right), \tag{25}$$

where

$$A(r)=\frac{1}{r}\left(-\frac{\beta}{\alpha+\beta \ln r}\right). \tag{26}$$

If one approximates Ψ_s with $(\alpha+\beta \ln r)f(k_a(r-t))$, the radiation boundary condition is

$$\frac{\partial \Psi_s}{\partial r}+\frac{\partial \Psi_s}{\partial t}+A(r)\Psi_s=0, \tag{27}$$

with a truncation error on the order of $1/r^2$.

3.3. *Boundary Condition for Time-Harmonic Waves*

Normally, the waves are cylindrically expanding in the far field, i.e., large $k_a r$. In eddy current situations, $k_a=O(10^{-7})$. In order to reach the far field, one must consider a distance $r>10^7$. This makes the computation impossible. What is presented here is a heuristic idea that contains two observations. One is that for low-frequency waves, even in the near field the waves can be cylindrically symmetric, e.g., see Fig. 9. Thus, one might neglect the angular dependence of the scattered wave on the artificial boundary. The other one is that $k_a r$ is also small. With a conducting scatterer, the relation: $\mathrm{Re}(\Lambda_s e^{ik_a t})\approx cY_0(k_a r)$ can be shown, based on [17], to exist on the appropriate near-field (i.e., $k_a r\approx 0$) boundaries. Here Λ_s is the complex phasor of Ψ_s, i.e., $\mathrm{Re}(\Lambda_s)=\Psi_s$. Re is to take the real part of its argument, c is a constant, and Y_0 is the Bessel function of the second kind and of

order zero. Since $k_a r \approx 0$, using the small-argument approximation of Bessel's function, we obtain

$$\mathrm{Re}(\Lambda_s e^{ik_a t}) \approx \frac{2c}{\pi}\left[\gamma + \ln\frac{k_a}{2}\right] + \frac{2c}{\pi}\ln r, \tag{28}$$

where γ is Euler's constant. On the other hand, from our previous discussion, the scattered waves can be approximated in the following way: $\Lambda_s = (\alpha + \beta \ln r) e^{ik_a r} e^{-ik_a t}$. Thus

$$\mathrm{Re}(\Lambda_s e^{ik_a t}) = (\alpha + \beta \ln r)\,\mathrm{Re}(e^{ik_a r}). \tag{29}$$

For $k_a r \approx 0$, $\mathrm{Re}(e^{ik_a r}) \approx 1$. Therefore from Eq. (28) and (29), we obtain the following approximations:

$$\alpha = \frac{2c}{\pi}\left(\gamma + \ln\frac{k_a}{2}\right) \qquad \text{and} \qquad \beta = \frac{2c}{\pi}.$$

Substituting these in (26), we obtain the radiation boundary condition for low-frequency time-harmonic waves,

$$\frac{\partial \Psi_s}{\partial r} + \frac{\partial \Psi_s}{\partial t} + A(r)\,\Psi_s = 0, \tag{30}$$

where

$$A(r) = \frac{1}{r}\left[-\frac{1}{\gamma + \ln k_a - \ln 2 + \ln r}\right]. \tag{31}$$

Compared to the radiation conditions in literature, (27) and (30) are classified as the first-order conditions. However, they are derived through the assumption of small $k_a r$. This near-field feature enables their radiation boundaries to move very close to the interface boundary. For example, when a single circular conductor is used as the scatterer, (30) can be posed on a boundary which is only two grid spacings away from the interface boundary (see Section 5). Also, for low-frequency waves, it is easy to verify that $A(r)$ is positive. With (27) and (30) imposed on the exterior boundary, the problem becomes well-posed. The proof for the uniqueness of the solution is shown in Appendix A.

The boundary condition (30) contains a frequency-dependent parameter k_a. This suggests that the radiation condition for low-frequency situations is frequency dependent. However, there is some range for the boundary condition to move. When k_a is very small, probably due to low frequency or small L, the variation of $A(r)$ within a small range of frequencies might be negligible. In that case, $A(r)$ for the central frequency can be used for the multi-frequency problem. Our recent research is concentrated on this aspect. The result will be reported later. For the

problems involved with a wide range of frequencies, this procedure calls for modifications to the boundary condition (30). From the incident field, it is possible to estimate the low-frequency contents of the problem by considering the Fourier spectrum. In this case, $A(r)$ as defined in (31) should be obtained for each low-frequency component. For frequencies above the cut off limit, $A(r)$ should be replaced by $1/(2r)$ as noted in Eq. (14).

4. Finite Difference Formulation of the Problem

The radiation conditions in the previous section can be easily integrated into the finite difference scheme. The finite difference formulae used in solving this problem are summarized below. Note that the spatial differences in both x and y directions are chosen to be equal, i.e., $\Delta x = \Delta y$. The superscript "i" represents the time coordinate and the subscripts "j" and "k" represent the grid coordinates in the x and y directions, respectively.

The following central-difference forula is used to discretize equation (10):

$$\Psi_{j,k}^{i+1} = 2\Psi_{j,k}^{i} - \Psi_{j,k}^{i-1} + \left(\frac{\Delta t}{\Delta x}\right)^2 \times (\Psi_{j+1,k}^{i} + \Psi_{j-1,k}^{i} + \Psi_{j,k+1}^{i} + \Psi_{j,k-1}^{i} - 4\Psi_{j,k}^{i}) \quad \text{in } \Omega_A. \tag{32}$$

Similarly, the difference formula is obtained for Eq. (11),

$$\Psi_{j,k}^{i+1} = a\Psi_{j,k}^{i} - b\Psi_{j,k}^{i-1} + c(\Psi_{j+1,k}^{i} + \Psi_{j-1,k}^{i} + \Psi_{j,k+1}^{i} + \Psi_{j,k-1}^{i} - 4\Psi_{j,k}^{i}) \quad \text{in } \Omega, \tag{33}$$

where

$$a = 2\Big/\left(1 + \frac{l_m^2}{2k_m^2}\Delta t\right), \qquad b = \left(1 - \frac{l_m^2}{2k_m^2}\Delta t\right)\Big/\left(1 + \frac{l_m^2}{2k_m^2}\Delta t\right),$$

$$c = \left(\frac{1}{k_m^2}\left(\frac{\Delta t}{\Delta x}\right)^2\right)\Big/\left(1 + \frac{l_m^2}{2k_m^2}\Delta t\right).$$

On the radiation boundary, the total wave consists of two components: the incident wave Ψ_{inc} and the scattered wave Ψ_s, i.e., $\Psi = \Psi_{\text{inc}} + \Psi_s$. The radiation condition takes care of the scattered wave only. The origin is located at the center of the scatterer as shown in Fig. 1(b). Using the derivatives in Cartesian coordinates, the radiation condition has the following form:

$$\frac{\partial \Psi_s}{\partial x}\cos\theta + \frac{\partial \Psi_s}{\partial y}\sin\theta + \frac{\partial \Psi_s}{\partial t} + A(r)\Psi_s = 0. \tag{34}$$

Finite difference methods usually yield difficulties at the corners of a rectangular radiation boundary. These are due to the conflicts of difference formulae at the corners. As a result, these corners become the sources of instability. To avoid the

corner problems, [18] proposed a different boundary condition be used for the two grid points nearest to the corners. Unfortunately, this procedure yields complication. In our experiment, a method using a smooth transition was developed to solve the corner problems. The approach is depicted in Fig. 1(c). On the left boundary, A_0 is the central grid point, A_1 the nearest grid point above A_0, A_{-1} the nearest grid point below A_0. On the right boundary, B_0 is the central grid point, B_1 the nearest grid point above B_0, and B_{-1} the nearest grid point below B_0. On the top boundary, C is the central grid point, A_2 the nearest grid point to the left of C, and B_2 the nearest grid point to the right of C. On the bottom boundary, C' is the central grid point, A_{-2} the nearest grid point to the left of C', and B_{-2} the nearest grid point to the right of C'. The scheme is explained as follows. On the boundary A_1 to A_2, $\partial \Psi_s/\partial x$ is implemented by a forward-difference formula and $\partial \Psi_s/\partial y$ is implemented by a backward-difference formula. On the boundary B_1 to B_2, $\partial \Psi_s/\partial x$ and $\partial \Psi_s/\partial y$ are both implemented by the backward-difference methods. It seems that the implementations of $\partial \Psi_s/\partial x$ on two boundaries will conflict at the intersection grid point C. But, since the term is multiplied by $\cos\theta$ and its value is 0 at C, the conflict will not take effect and the corner problems are avoided. The following difference formulae are used to discretize the radiation condition (34) on the upper radiation boundary:

$$(\Psi_s)_{j,k}^{i+1} = d(\Psi_s)_{j,k}^{i} - g[(\Psi_s)_{j+1,k}^{i} - (\Psi_s)_{j,k}^{i}] \quad \text{at } A_0, \tag{35}$$

$$(\Psi_s)_{j,k}^{i+1} = d(\Psi_s)_{j,k}^{i} - g[(\Psi_s)_{j+1,k}^{i} - (\Psi_s)_{j,k}^{i}] - h[(\Psi_s)_{j,k}^{i} - (\Psi_s)_{j,k-1}^{i}] \quad \text{on } A_1 - A_2, \tag{36}$$

$$(\Psi_s)_{j,k}^{i+1} = d(\Psi_s)_{j,k}^{i} - h[(\Psi_s)_{j,k}^{i} - (\Psi_s)_{j,k-1}^{i}] \quad \text{at } C, \tag{37}$$

$$(\Psi_s)_{j,k}^{i+1} = d(\Psi_s)_{j,k}^{i} - g[(\Psi_s)_{j,k}^{i} - (\Psi_s)_{j-1,k}^{i}] - h[(\Psi_s)_{j,k}^{i} - (\Psi_s)_{j,k-1}^{i}] \quad \text{on } B_1 - B_2, \tag{38}$$

$$(\Psi_s)_{j,k}^{i+1} = d(\Psi_s)_{j,k}^{i} - g[(\Psi_s)_{j,k}^{i} - (\Psi_s)_{j-1,k}^{i}] \quad \text{at } B_0. \tag{39}$$

The condition on the lower boundary is handled by a symmetry to the upper boundary. The coefficients d, g, and h are defined as:

$$d = 1 - \frac{\Delta t}{\Delta x} A(r), \qquad g = \cos\theta \frac{\Delta t}{\Delta x}, \qquad h = \sin\theta \frac{\Delta t}{\Delta x},$$

where $A(r)$ is defined by Eq. (31). Note that in Eq. (35)–(39), the terms with coefficients g and h take care of the derivatives in Eq. (34), and the terms with the coefficient d take care of the term of $A(r)$.

Numerical implementation of the interface conditions needs special attention. In Ref. [19], interface conditions are implemented by a cell integration method. Here we present a simple way to solve it directly using the finite-difference methods. Our approach uses an idea of fictitious fields. This idea was also found in [20] for the

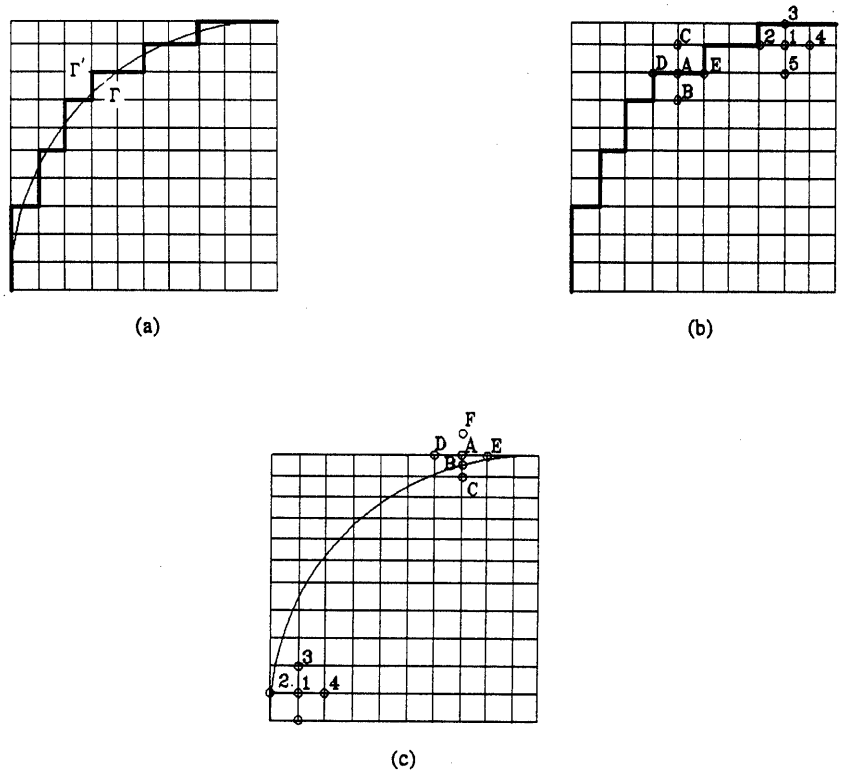

FIG. 2. (a) Approximating a curve Γ with a polygon Γ'. (b) Grid points near the interface boundary when $\mu_r \neq 1$. (c) Grid points near the interface boundary when $\mu_r = 1$.

vector field code. As suggested in [21], an interface boundary with some extent of curvature can be approximated by a stair geometry with its vertices occupying the regular grid points. For example, the circle in Fig. 2(a) can be approximated by the polygon Γ'. Then the field computation is classified into two categories: exterior (air) and interior (conductor). For the grid points on the boundary, to obtain an accurate result, the following are suggested. When the grid separation is much larger than the estimated skin depth, the interior wave equation is used. When the grid separation is equal to or smaller than the estimated skin depth, the exterior wave equation is used. The second interface condition $\partial\Psi^-/\partial n = \partial\Psi^+/\partial n$ can be transformed into

$$\frac{\partial\Psi^-}{\partial x}\cos\theta + \frac{\partial\Psi^-}{\partial y}\sin\theta = \frac{\partial\Psi^+}{\partial x}\cos\theta + \frac{\partial\Psi^+}{\partial y}\sin\theta, \tag{40}$$

where θ is the angle between the normal direction and the x-axis. From this condition, when the field computation involves a point in the other region, the following

local approximations are used: $\partial\Psi^-/\partial x = \partial\Psi^+/\partial x$ and $\partial\Psi^-/\partial y = \partial\Psi^+/\partial y$. With these, when the field computations involves a grid point in the other region, a fictitious field at that point can be obtained for computation. For the following explanations, the wave equation in the air is assumed for the grid points on the boundary. In Fig. 2(b), the field computation at A belongs to the category of the air. But a grid point B in the conductor is involved in the difference formula as shown below:

$$\Psi_A^{i+1} = 2\Psi_A^i - \Psi_A^{i-1} + \left(\frac{\Delta t}{\Delta x}\right)^2 ((\Psi_B^*)^i + \Psi_C^i + \Psi_D^i + \Psi_E^i - 4\Psi_A^i), \tag{41}$$

where Ψ_B^* is the fictitious field at B, i.e., the field value at B, if the air covers the whole space. From the local approximation to the second interface condition, $\Psi_B^* - \Psi_A = \Psi_B - \Psi_A^+$. Furthermore, from the first interface condition, $\Psi_A^+ = 1/\mu_r \Psi_A$. Thus, $\Psi_B^* = \Psi_B + (1 - 1/\mu_r)\Psi_A$. Substituting into Eq. (41), we obtain

$$\Psi_A^{i+1} = 2\Psi_A^i - \Psi_A^{i-1} + \left(\frac{\Delta t}{\Delta x}\right)^2 (\Psi_B^i + \Psi_C^i + \Psi_D^i + \Psi_E^i - (3 + 1/\mu_r)\Psi_A^i). \tag{42}$$

Similarly, using the first interface condition, the field at point 1 can be calculated from

$$\Psi_1^{i+1} = a\Psi_1^i - b\Psi_1^{i-1} + c(\Psi_2^i/\mu_r + \Psi_3^i/\mu_r + \Psi_4^i + \Psi_5^i - 4\Psi_1^i), \tag{43}$$

where a, b, and c are the same constants as those in Eq. (33).

If the relative permeability μ_r of the conductor is 1, approximating the interface boundary with a stair geometry becomes unnecessary. When a field computation involves a grid point in the other region, the real field value at that point will be used directly for calculation because it aproximates the fictitious value. For example, in Fig. 2(c), from the local approximation to the second interface condition, $(\Psi_C^* - \Psi_B^-)/s = (\Psi_C - \Psi_B^-)/s$, where s is the distance between B and C. From the first interface condition, $\Psi_B^- = \Psi_B^+$. Thus $\Psi_C^* = \Psi_C$. As a result, the field at A can be obtained from the formula

$$\Psi_A^{i+1} = 2\Psi_A^i - \Psi_A^{i-1} + \left(\frac{\Delta t}{\Delta x}\right)^2 (\Psi_C^i + \Psi_D^i + \Psi_E^i + \Psi_F^i - 4\Psi_A^i). \tag{44}$$

Similarly, the field at the grid point 1 can be calculated from the formula

$$\Psi_1^{i+1} = a\Psi_1^i - b\Psi_1^{i-1} + c(\Psi_2^i + \Psi_3^i + \Psi_4^i + \Psi_5^i - 4\Psi_1^i). \tag{45}$$

5. Numerical Experiments

For the following numerical experiments, the incident waves are assumed to be the sinusoidal TM plane waves, propagating in the x direction. These waves are

incident on the left boundary starting at $t=0$. Therefore, the incident component of the field at the grid point (j, k) is $(\Psi_{\text{inc}})^i_{j,k} = \cos[k_a(i\,\Delta t - j\,\Delta x)]$.

5.1. *Experiment I*

To validate the new radiation condition (30), we have the first numerical experiment as follows. The conductor is assumed to be a circular cylinder made of aluminium. The grid coordinates with the parameters used are shown in Fig. 3. The incident wave has a frequency of 60 Hz. The associated parameters $k_a = 2.514987 \times 10^{-7}$, $l_m^2 = 2.802903 \times 10^9$, and $k_m^2 = 1$. We used $\Delta t = 0.09256006$ (the real time interval is 6.174877×10^{-11} s), and $\Delta x = 0.1308997$ (the real space separation is 2.617994×10^{-2} m). With these choices, $(\Delta t/\Delta x)^2 = 0.4999999 < 0.5$. Courant's stability criterion for Eq. (10) is satisfied. Since l_m^2 is very large, the stability criterion for (11) is mainly posed on the k_m^2 term. Therefore our choices of Δt and Δx also satisfy the stability criterion for (11). The numerical methods presented above were implemented in a computer program, running on a SUN 4/260 workstation. The numerical solution using the low-frequency radiation condition (see Fig. 4), was obtained after 67,900 time steps. This is equivalent to 2.515645×10^{-4} period. The CPU time is about 1.5 h. From the history plot at a point (67,34) (see Fig. 7), the solution in the exterior region is found to be in a transient state but with a value almost approaching that at the steady state. For comparison, the numerical solution using the radiation condition (14) was also obtained and is shown in Fig. 5.

To obtain the analytic solution, we assume the solution of Eq. (10) and (11) to be $\Lambda = R(r)\,\Theta(\theta)e^{-ik_a t}$. Here, Λ is the complex phasor of Ψ, i.e., $\Psi = \text{Re}(\Lambda)$. Separation of variables on Eq. (10) and (11) yields the analytic forms

$$\Lambda^-(r, \theta, t) = \sum_{n=0}^{\infty} i^n \varepsilon_n \cos(n\theta)[J_n(k_a r) + a_n H_n^{(1)}(k_a r)]\, e^{ik_a x_L} e^{-ik_a t}, \tag{46}$$

$$\Lambda^+(r, \theta, t) = \sum_{n=0}^{\infty} i^n \varepsilon_n \cos(n\theta)\, b_n J_n(pr)\, e^{ik_a x_L} e^{-ik_a t}, \tag{47}$$

where J_n is the Bessel function of the first kind and order n, $H_n^{(1)}$ is the Hankel function of the first kind and order n, and x_L is the distance from the center of the cylinder to the left boundary. $\varepsilon_0 = 1$ and $\varepsilon_n = 2$ for $n \geqslant 1$. Through variable separation on (11), we obtain $p = \sqrt{\omega^2 L^2 \mu_m \varepsilon_m + i\omega L^2 \sigma_m \mu_m} \approx \sqrt{i\omega L^2 \sigma_m \mu_m}$. Using the interface conditions, the coefficients a_n and b_n are determined from the equations

$$J_n(k_a a) + a_n H_n^{(1)}(k_a a) = \mu_r b_n J_n(pa), \tag{48}$$

$$k_a[J_n'(k_a a) + a_n (H_n^{(1)})'(k_a a)] = b_n p J_n'(pa), \tag{49}$$

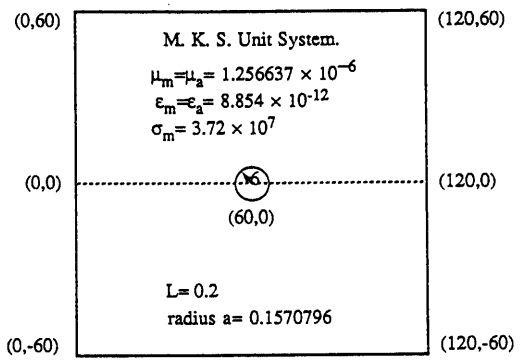

FIG. 3. Grid size and important parameters for numerical experiment I.

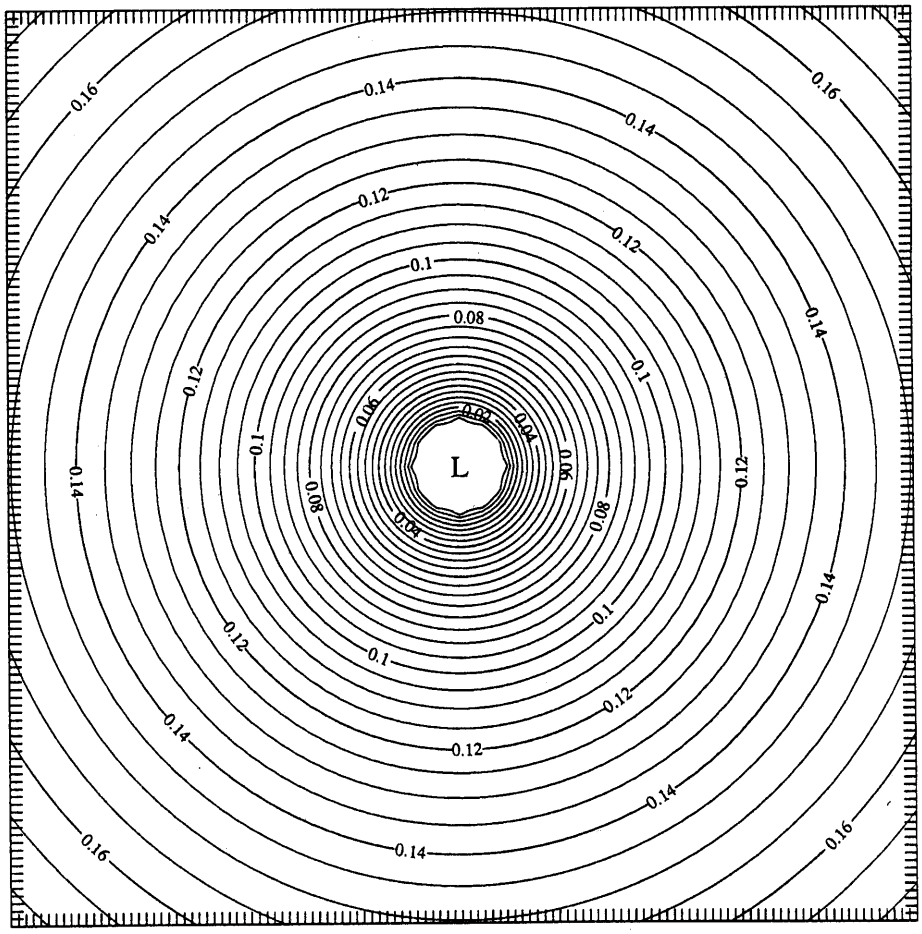

FIG. 4. Contour plot of the numerical solution in experiment I, using the boundary condition (30). The result was obtained after 2.515645×10^{-4} period from the beginning.

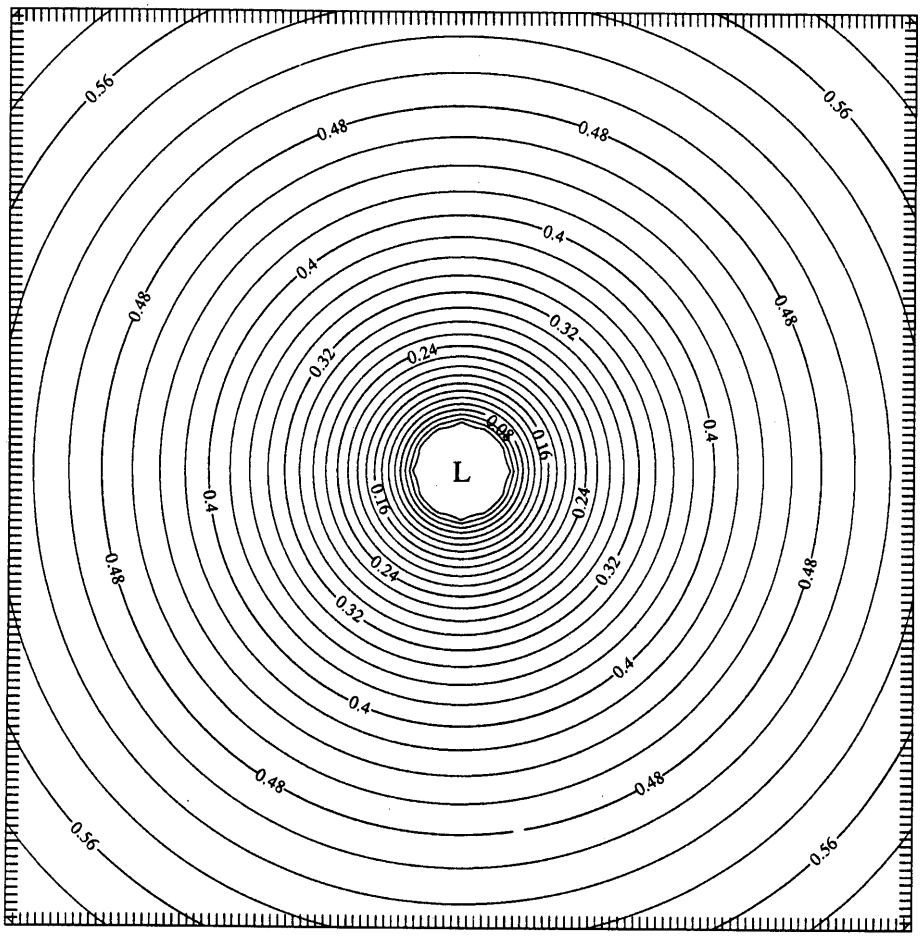

FIG. 5. Contour plot of the numerical solution in experiment I, using the radiation boundary condition (14). The result was obtained after 2.515645×10^{-4} period from the beginning.

for $n = 0, 1, 2, \ldots$, where a is the radius of the cylinder. The first three coefficients in these two equations are calculated to be

$$a_0 = -1.027247 \times 10^{-2} - i9.971206 \times 10^{-2}$$
$$a_1 = -2.004432 \times 10^{-15} - i2.852592 \times 10^{-14}$$
$$a_2 = -1.817832 \times 10^{-29} - i1.288663 \times 10^{-28}$$
$$b_0 = -1.106546 \times 10^{-8} + i8.582522 \times 10^{-9}$$
$$b_1 = 2.314644 \times 10^{-14} + i3.575007 \times 10^{-14}$$
$$b_2 = 3.629113 \times 10^{-21} - i2.260305 \times 10^{-21}.$$

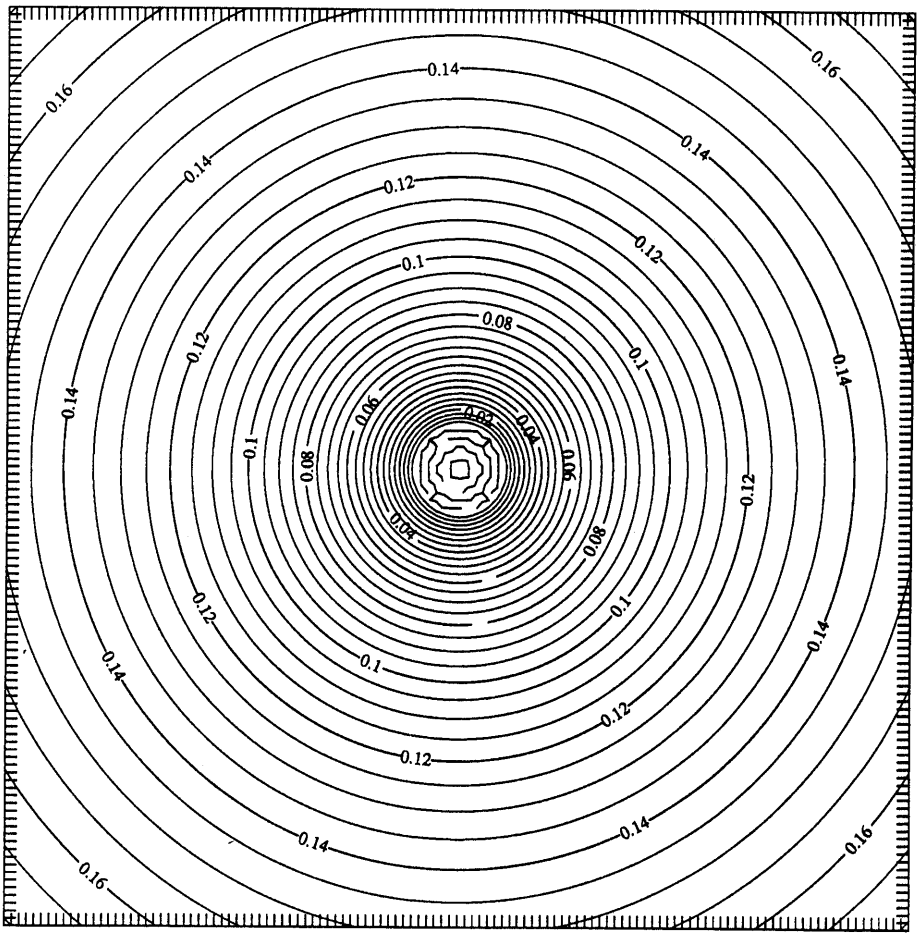

FIG. 6. Contour plot of the analytic solution in experiment I. The result was obtained from Eq. (46) and (47) by setting $k_a t = 2.515645 \times 10^{-4} \times 2\pi$.

Taking the first three terms in the series, we plot the analytic solution in Fig. 6. Comparing this to Fig. 5, we find that the numerical solution using the radiation condition (14) has a large numeric error although its field pattern is similar to that of the analytic solution. The error comes from the position where the radiation condition is applied. This condition requires $k_a r$ to be large. But in this experiment, $k_a r$ is very small ($O(10^{-6})$). As a result, the error appeares to be large. On the other hand, if we expand the computation domain to get a large $k_a r$, the grid size will become too large to be implemented on a computer. Therefore the boundary condition (30), which is appropriate to the case of small $k_a r$, is needed to solve the problem (Fig. 7).

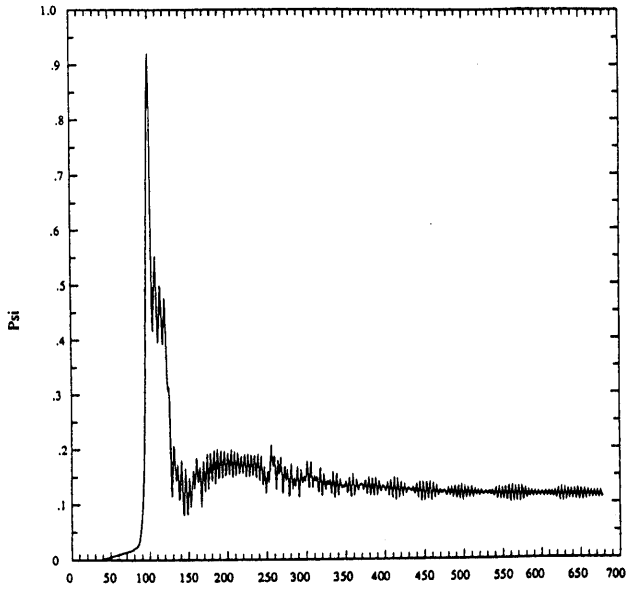

(a)

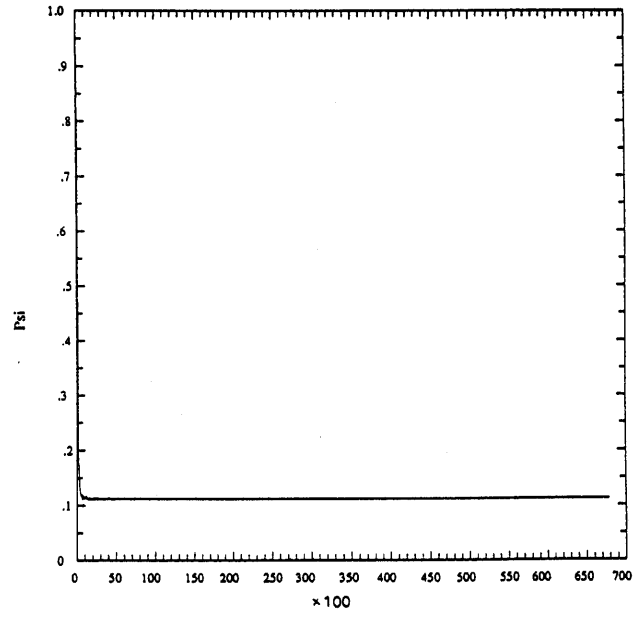

(b)

FIG. 7. History plot at $P(67, 34)$ in numerical experiment I. (a) Plot for the beginning 679 time steps. (b) Plot from the beginning through 67,900 time steps.

TABLE I

Comparison of Solutions in Experiment I, in Double Precision Expression

Radius	Grid	Numerical	Analytic
20	(80, 0)	0.8035427D-01	0.7879715D-01
	(74, 14)	0.7969991D-01	0.7815606D-01
	(60, 20)	0.8028407D-01	0.7879725D-01
	(45, 14)	0.8197310D-01	0.8042111D-01
	(40, 0)	0.8021339D-01	0.7879735D-01
40	(100, 0)	0.1246082D+00	0.1227901D+00
	(88, 28)	0.1239659D+00	0.1221490D+00
	(60, 40)	0.1245336D+00	0.1227901D+00
	(31, 28)	0.1250927D+00	0.1232822D+00
	(20, 0)	0.1244591D+00	0.1227902D+00
60	(120, 0)	0.1503752D+00	0.1485242D+00
	(102, 42)	0.1498472D+00	0.1478831D+00
	(60, 60)	0.1503764D+00	0.1485243D+00
	(17, 42)	0.1505956D+00	0.1486387D+00
	(0, 0)	0.1503784D+00	0.1485243D+00
4	(64, 0)	0.1710767D-13	0.2201674D-04
	(62, 2)	0.1975745D-18	-0.1127474D-05
	(60, 4)	0.1719809D-13	0.2201422D-04
	(57, 2)	0.3046863D-14	0.1069381D-04
	(56, 0)	0.1731365D-13	0.2201171D-04

Comparison of Figs. 4 and 6 shows that the numerical solution, using the low-frequency radiation condition (30), matches the analytic solution very well in the exterior region. Both solutions, numerical and analytic, at the points with $r = 4$, 20, 40, 60 and $\theta = 0$, $\pi/4$, $\pi/2$, $3\pi/4$, π are listed in Table I. From this table, two solutions in the exterior region are found in excellent agreement. This proves that the new radiation boundary condition (30) works very well for low-frequency electromagnetic waves. It is also shown in this table that the fields on the

illuminated and the shadowed sides are nearly the same because of the strong diffraction of low-frequency waves. The root mean square error for the whole computational domain is calculated to be 1.39%. Equations (46) and (47) show that the analytic solution is at a sinusoidal steady state. However, the numerical solution is in a transient state, i.e., the field is still on its way penetrating into the conductor. This explains the difference of the inside field between two solutions.

5.2. *Experiment II*

In this experiment we focus on the accuracy of the solution in the interior region. To capture the accurate eddy current phenomenon, a grid separation, which is

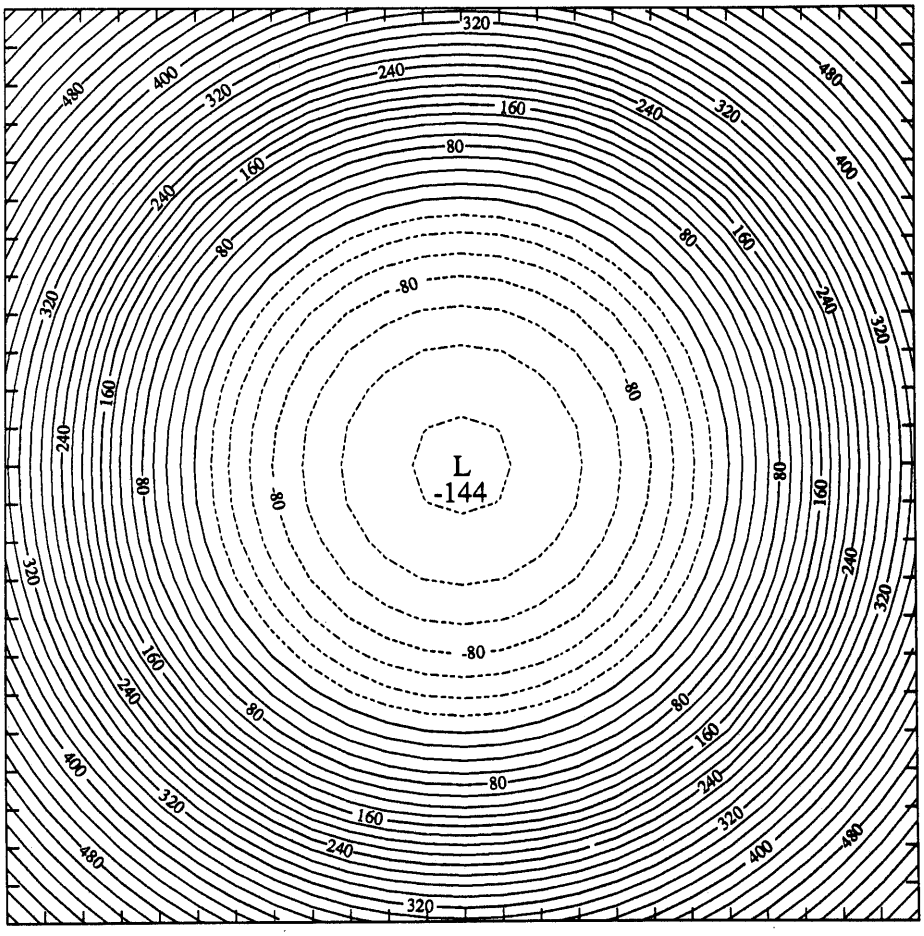

FIG. 8. Contour plot of the numerical result in Experiment II. The result was obtained after one period from the beginning.

about $\frac{1}{5}$ of the estimated skin depth, is chosen for this experiment. This skin depth is defined, in the case of a plane scatterer of infinite depth, as:

$$\delta = \sqrt{1/\pi f \mu_m \sigma_m}, \tag{50}$$

where f is the frequency of the incident wave, and μ_m and σ_m are the permeability and conductivity of the scatterer, respectively. The conductor in this experiment is assumed to be a circular cylinder made of graphite with the radius, $a = 6.544985 \times 10^{-2}$ m, $\sigma_m = 4 \times 10^4$ S/M, $\mu_m = \mu_a$, and $\varepsilon_m = \varepsilon_a$. The frequency of the incident wave is 6000 Hz. Therefore, the estimated skin depth is 3.248737×10^{-2} m. The grid size is 25×25 with the diameter of the conductor occupying 21 grid points.

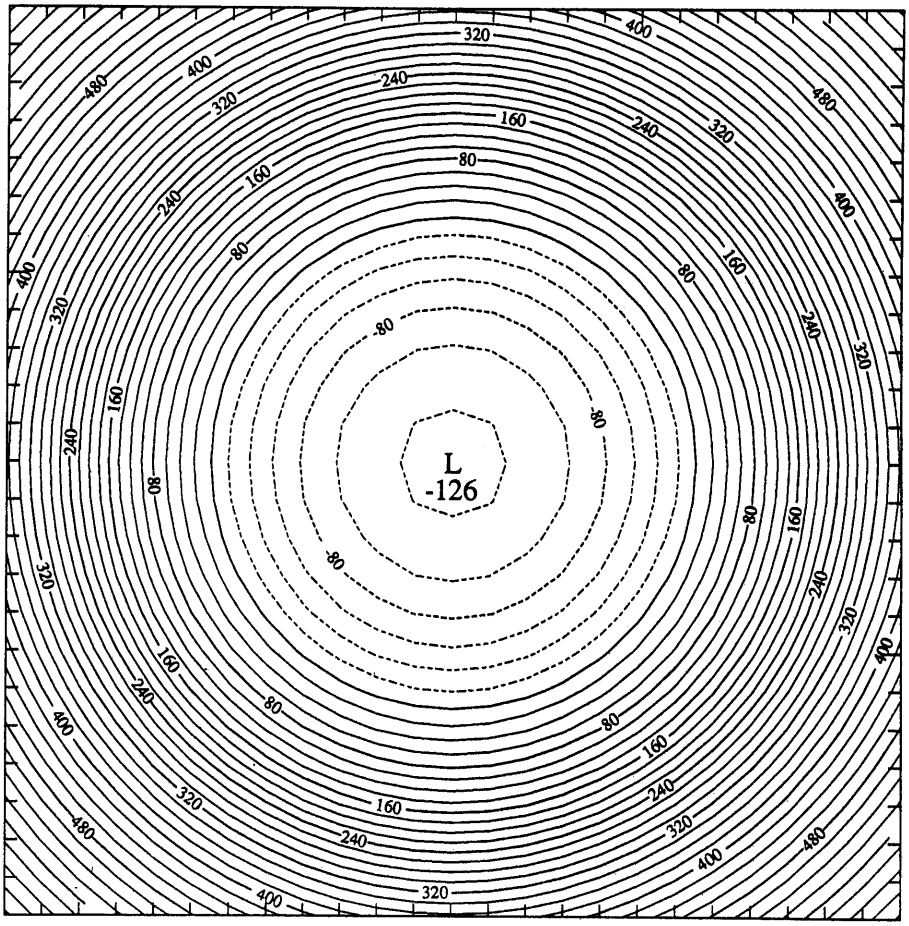

FIG. 9. Contour plot of the analytic solution in Experiment II. The result was obtained from Eq. (46) and (47) by setting $k_a t = 2\pi$.

The length L for space scaling is 0.05 m. The associated parameters $k_a = 6.287468 \times 10^{-6}$, $l_m^2 = 7.534687 \times 10^5$, and $k_m^2 = 1$. We used $\Delta t = 0.09256006$ (the real time interval is 1.543719×10^{-11} s and $\Delta x = 0.1308997$ (the real space separation is 6.544985×10^{-3} m). Figure 8 shows the numerical result after one period. The calculation took 10.8×10^6 time steps (20 min CPU time on a CRAY-XMP-24). Compared to the analytic solution in Fig. 9, the numerical result is found to be satisfactory. Figure 8 demonstrates a clear eddy current phenomenon, i.e., the field distribution inside the conductor is concentrated in a region near the boundary and decay rapidly beyond this region.

In Fig. 10 the time history of the solution at a point $P(3, 0)$ inside the conductor is shown. Initially, only the left boundary was excited by the incident wave. The field values at other locations were all zero. Then, the wave propagates towards the interface boundary and penetrates into the conductor. As a result, the field value at $P(3, 0)$ is attained in a waveform similar to the incident wave, as shown in Fig. 10. This is different from the quasi-static field. Quasi-static fields can exhibit the sinusoidal time variation but may not be the traveling waves. However, our numeri-

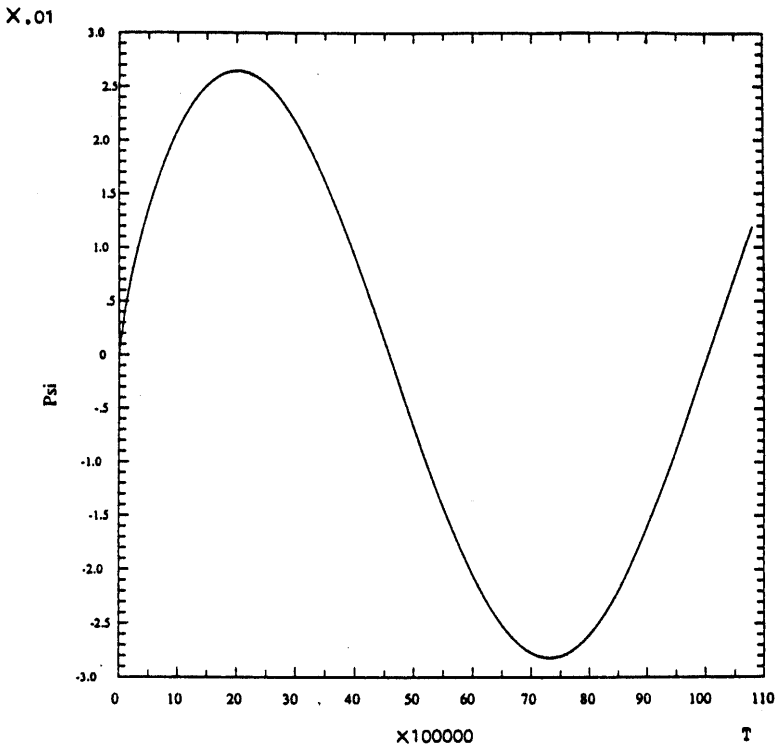

FIG. 10. History plot at $P(3, 0)$, which is inside the conductor, in experiment II. The plot is from the beginning through 10.8×10^6 time steps, i.e., one period.

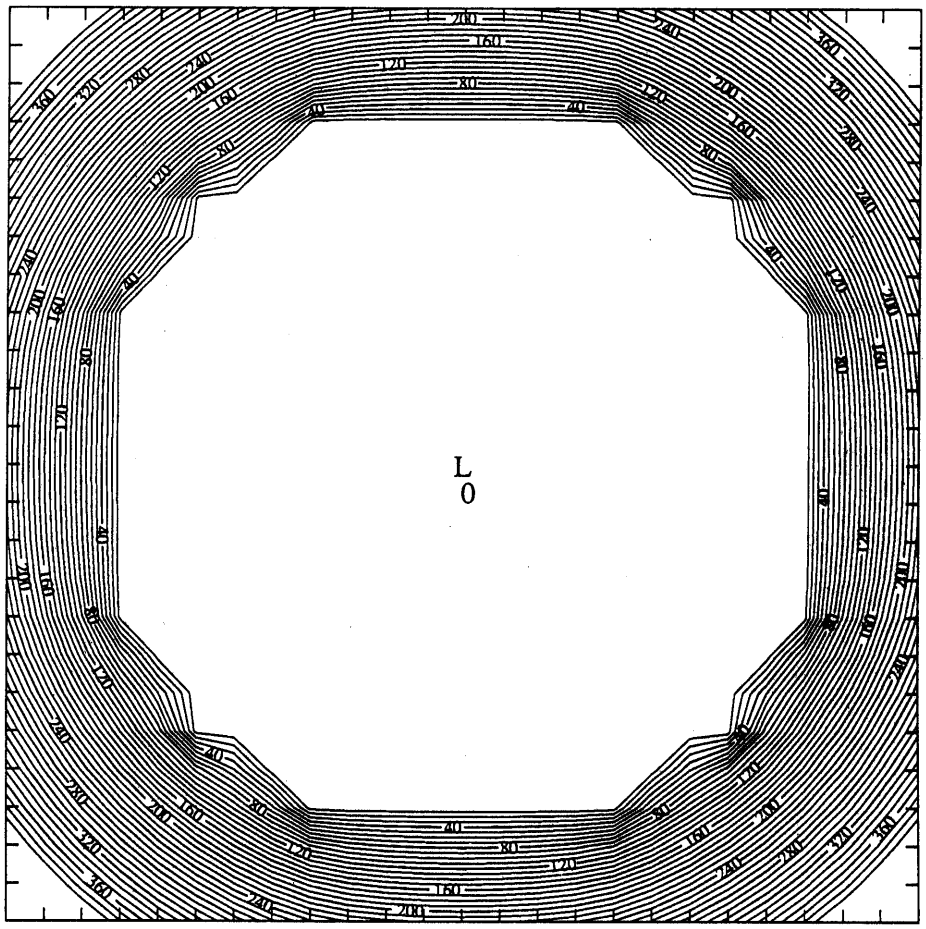

(a)

FIG. 11. Contour plots in Experiment II. The unit for each contour line is 0.01. (a) After 5000 time steps. (b) After 100,000 time steps. (c) After 200,000 time steps.

cal results show the fields traveling in the conductor, see Fig. 11. Figure 11(a) shows the field distribution after 5000 time steps. The visible fields exist within the first grid points inside the boundary. Figure 11(b) shows the field distribution after 100,000 time steps. The visible fields, at this time, have moved forward. Figure 11(c) shows the field distribution after 200,000 time steps. The visible fields are found to move further. Also, the wavefront outside the conductor, e.g., the line $\Psi = 360(\times 10^{-2})$, is found moving. This phenomenon of traveling wave justifies the comment we made earlier. Both regions are governed by a wave phenomenon.

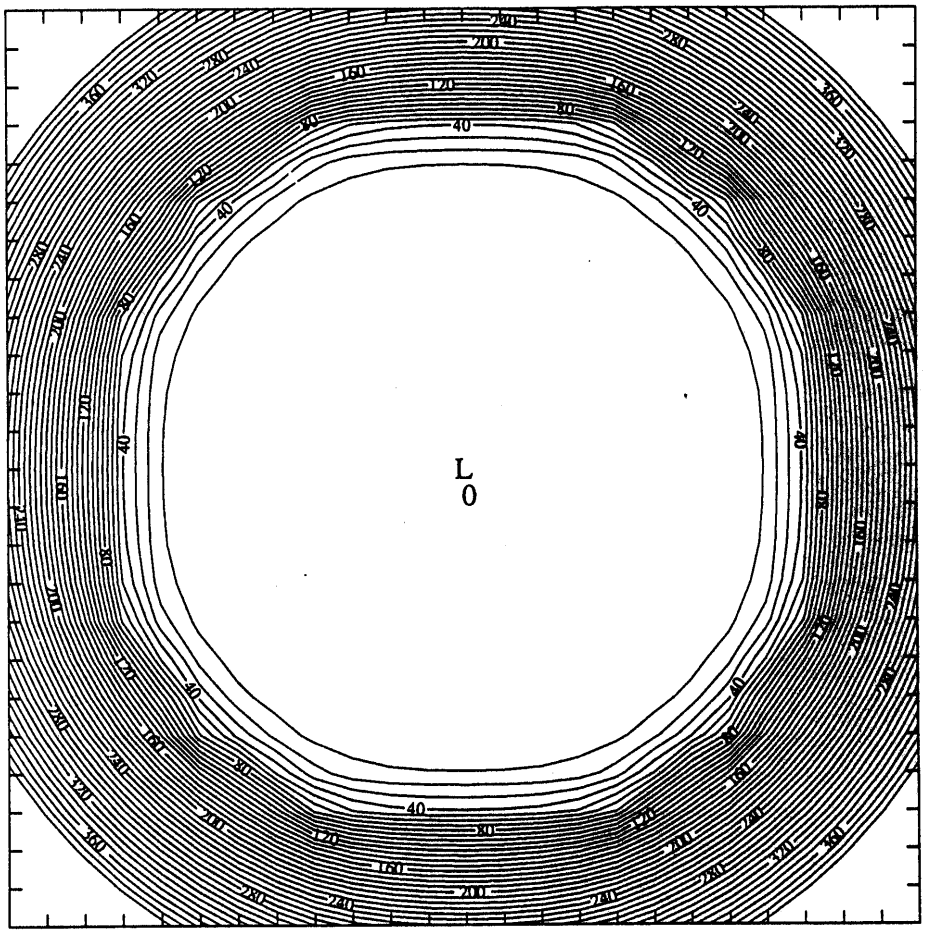

(b)

FIG. 11—*Continued*

5.3. *Experiment III*

In this experiment, we refine the grid mesh in Experiment II. The physical conditions are kept the same, but the grid interval is refined to half that in the previous experiment. The grid size is now 49×49 with the conductor's diameter occupying 41 grid points. The length L used for space scaling is 0.025 m. The associated parameters $k_a = 3.143734 \times 10^{-6}$, $l_m^2 = 3.767344 \times 10^5$, and $k_m^2 = 1$. We used $\Delta t = 0.09256006$ (the real time interval is 7.71859×10^{-12} s), and $\Delta x = 0.1308997$ (the real space separation is 3.272493×10^{-3} m). The numerical result for a period was obtained after 21.6×10^6 time steps. Table II shows the comparison of this result to that in the previous experiment. No big differences are found between the

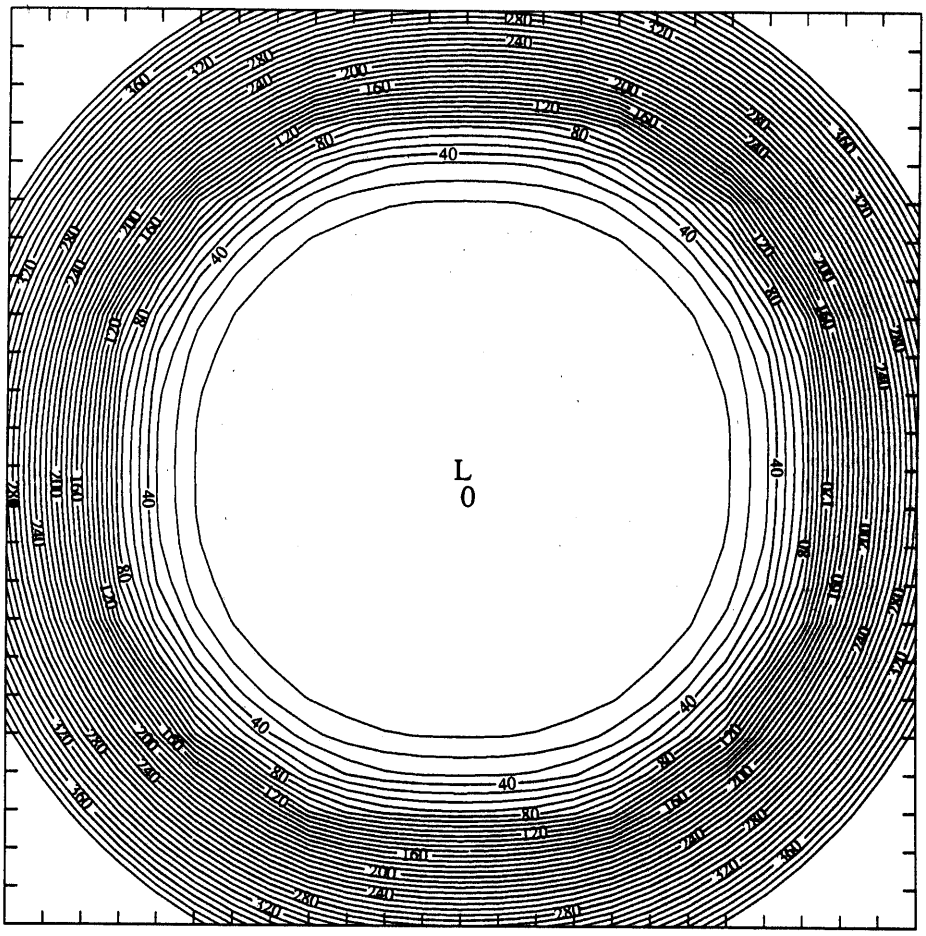

(c)

FIG. 11—*Continued*

two results, showing the stability of the scheme. Figure 12 shows the numerical result for the time instant at a quarter period. At this time, the incident magnetic field becomes identically zero. However, from Fig. 12, we find that a weak magnetic field still exists in the exterior region. At the beginning, the field penetrates from the exterior region into the interior region. At the time near a quarter cycle, the interior field is so much stronger than the exterior field that it penetrates back to the exterior region through the interface conditions. Therefore the maximum value of Φ occurs inside the conductor at this time. For a general transient signal, the problem must be solved in the time domain, where this phenomenon is more understandable, rather than in the frequency domain.

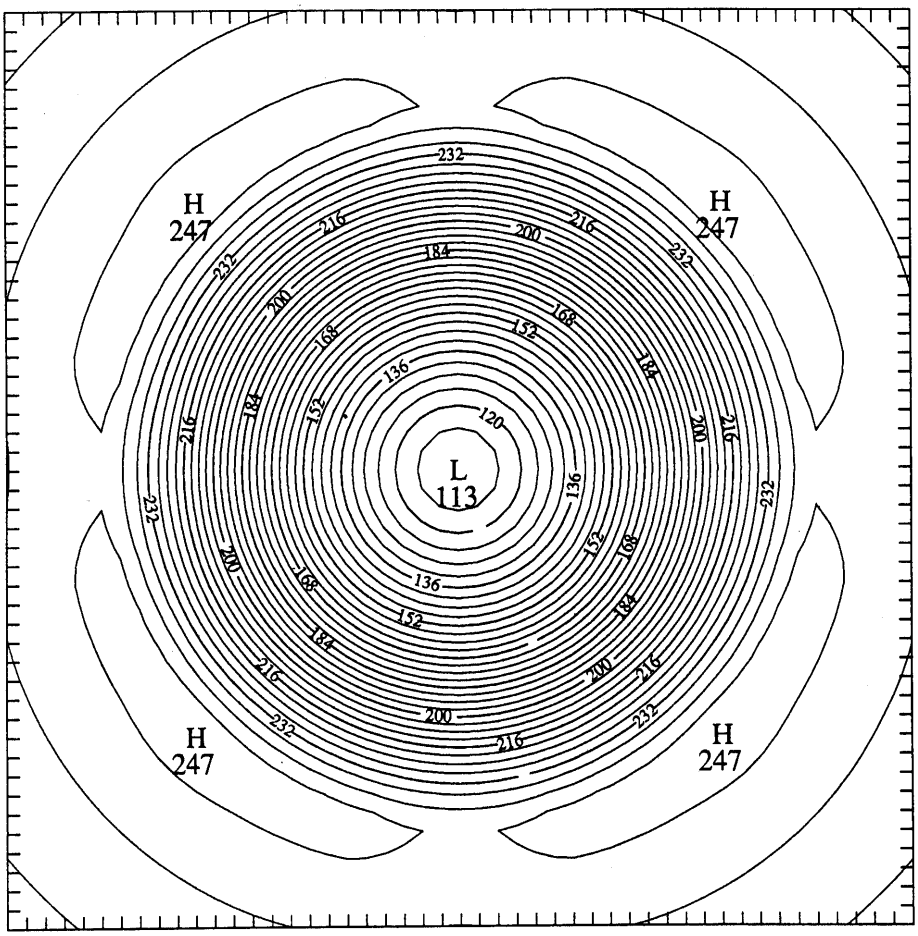

FIG. 12. Contour plot of the numerical solution at a quarter period in Experiment III.

6. CONCLUDING REMARKS

From our investigation, the following conclusions are reached:

1. Time-stepping of potential functions, for electromagnetic wave propagation and scattering problems, is feasible.

2. To solve the eddy current problems, a boundary condition (30) which is appropriate to the case of small $k_a r$ is obtained. Our numerical experiments have shown that it works very well.

3. Calculation of low-frequency penetration fields into a good conductor has been successfully achieved.

TABLE II

Comparison of Solutions in Experiments II and III, in Double Precision Expression

Experiment II		Experiment III	
Position	Field Value	Position	Field Value
(0, 12)	0.6302000D-01	(0, 24)	0.6240490D-01
(2, 10)	0.4789700D-01	(4, 20)	0.4727480D-01
(4, 8)	0.2942620D-01	(8, 16)	0.2877390D-01
(6, 6)	0.7877070D-02	(12, 12)	0.7390440D-02
(8, 4)	-0.5976780D-02	(16, 8)	-0.6221140D-02
(10, 2)	-0.1255920D-01	(20, 4)	-0.1265110D-01
(12, 0)	-0.1441850D-01	(24, 0)	-0.1445360D-01
(14, -2)	-0.1256070D-01	(28, -4)	-0.1265260D-01
(16, -4)	-0.5979730D-02	(32, -8)	-0.6224050D-02
(18, -6)	0.7873060D-02	(36,-12)	0.7386450D-02
(20, -8)	0.2942230D-01	(40,-16)	0.2877000D-01
(22,-10)	0.4789330D-01	(44,-20)	0.4727110D-01
(24,-12)	0.6301640D-01	(48,-24)	0.6240130D-01

APPENDIX A: UNIQUENESS OF THE SOLUTION

The problem considered can be written in the following form:

$$\Psi^s_{tt} = \nabla^2 \Psi^s \quad \text{in } \Omega_A, \tag{51}$$

$$k_m^2 \Psi_{tt} + l_m^2 \Psi_t = \nabla^2 \Psi \quad \text{in } \Omega, \tag{52}$$

$$\Psi^s + \Psi^{inc} = \Psi \quad \text{on } \Gamma, \tag{53}$$

$$\frac{\partial \Psi^s}{\partial n} + \frac{\partial \Psi^{inc}}{\partial n} = \frac{\partial \Psi}{\partial n} \quad \text{on } \Gamma, \tag{54}$$

$$\Psi^s(x, y, 0),\ \Psi^s_t(x, y, 0) = 0 \quad \text{in } \Omega_A, \tag{55}$$

$$\Psi(x, y, 0),\ \Psi_t(x, y, 0) = 0 \quad \text{in } \Omega, \tag{56}$$

$$\Psi^s_r + \Psi^s_t + A(r)\Psi^s = 0 \quad \text{on } \Gamma_e. \tag{57}$$

Here ∇^2 is the Laplacian operator. Subscripts "t," "tt," and "r" represent the partial

derivatives. Superscripts "s" and "inc" represent the scattered wave and the incident wave respectively. Γ_e is the radiation boundary and assumed to be a circle here. $A(r)$ is defined in Eq. (26) and (31).

First, assume that the problem has two solutions $u_1(x, y, t)$ and $u_2(x, y, t)$ and $v(x, y, t) = u_2(x, y, t) - u_1(x, y, t)$. Then

$$v_{tt} = \nabla^2 v \qquad \text{in } \Omega_A, \tag{58}$$

$$k_m^2 v_{tt} + l_m^2 v_t = \nabla^2 v \qquad \text{in } \Omega, \tag{59}$$

$$v^- = v^+ \qquad \text{on } \Gamma, \tag{60}$$

$$\frac{\partial v^-}{\partial n} = \frac{\partial v^+}{\partial n} \qquad \text{on } \Gamma, \tag{61}$$

$$v(x, y, 0), v_t(x, y, 0) = 0 \qquad \text{in } \Omega_A, \Omega, \tag{62}$$

$$v_r + v_t + A(r)v = 0 \qquad \text{on } \Gamma_e. \tag{63}$$

We construct a function

$$E(t) = \frac{1}{2}\iint_{\Omega_A} (v_t^2 + \nabla v \cdot \nabla v)\, d\Omega_A + \frac{1}{2}\iint_{\Omega} (k_m^2 v_t^2 + \nabla v \cdot \nabla v)\, d\Omega, \tag{64}$$

where ∇ is the gradient operator and $\cdot$ is the operator for the inner product. Taking the derivative of $E(t)$ with respect to t, we obtain

$$\begin{aligned}
E'(t) &= \iint_{\Omega_A} (v_t v_{tt} + \nabla v \cdot \nabla v_t)\, d\Omega_A + \iint_{\Omega} (k_m^2 v_t v_{tt} + \nabla v \cdot \nabla v_t)\, d\Omega \\
&= \iint_{\Omega_A} (v_t \nabla^2 v + \nabla v \cdot \nabla v_t)\, d\Omega_A + \iint_{\Omega} (v_t \nabla^2 v + \nabla v \cdot \nabla v_t - l_m^2 v_t^2)\, d\Omega \\
&= \iint_{\Omega_A} (\nabla \cdot v_t \nabla v)\, d\Omega_A + \iint_{\Omega} (\nabla \cdot v_t \nabla v - l_m^2 v_t^2)\, d\Omega \\
&= \int_{S_A} v_t \nabla v \cdot \mathbf{n}\, ds + \int_{\Gamma} v_t \nabla v \cdot \mathbf{n}\, ds - \iint_{\Omega} l_m^2 v_t^2\, d\Omega \\
&= \int_{\Gamma_e} v_t v_n\, ds - \int_{\Gamma} v_t v_n\, ds + \int_{\Gamma} v_t v_n\, ds - \iint_{\Omega} l_m^2 v_t^2\, d\Omega \\
&= \int_{\Gamma_e} v_t v_n\, ds - \iint_{\Omega} l_m^2 v_t^2\, d\Omega \\
&= \int_{\Gamma_e} v_t v_r\, ds - \iint_{\Omega} l_m^2 v_t^2\, d\Omega \\
&= \int_{\Gamma_e} v_t(-v_t - A(r)v)\, ds - \iint_{\Omega} l_m^2 v_t^2\, d\Omega.
\end{aligned} \tag{65}$$

Thus we have

$$E'(t)+\int_{\Gamma_e} A(r)\, vv_t\, ds = -\int_{\Gamma_e} v_t^2\, ds - \iint_{\Omega} l_m^2 v_t^2\, d\Omega. \tag{66}$$

The right side of the equation above is less than or equal to zero. Then

$$E'(t)+\frac{\partial}{\partial t}\int_{\Gamma_e}\frac{1}{2}A(r)v^2\, ds \leqslant 0. \tag{67}$$

From the initial condition, $v(x, y, 0)=0$, $v_t(x, y, 0)=0$, and $E(0)=0$. It follows that

$$E(t)+\int_{\Gamma_e}\frac{1}{2}A(r)v^2\, ds \leqslant 0, \tag{68}$$

so that

$$E(t) \leqslant -\int_{\Gamma_e}\frac{1}{2}A(r)v^2\, ds. \tag{69}$$

From the structure of $A(r)$ (Section 3), $A(r)>0$ on Γ_e. As a result, $E(t)\leqslant 0$. But from the definition, $E(t)\geqslant 0$. Thus $E(t)=0$. This leads to $v_t(x, y, t)=0$, i.e., v is constant in time. Since $v(x, y, 0)=0$, $v(x, y, t)=0$ for all time and all space. This means $u_1(x, y, t)=u_2(x, y, t)$. Therefore we conclude that the problem has a unique solution.

ACKNOWLEDGMENTS

The authors wish to thank all three referees for constructive criticisms that led to the current version of this manuscript.

REFERENCES

1. S. I. HARIHARAN AND R. C. MACCAMY, *J. Comput. Phys.* **45**, 81 (1982).
2. R. C. MACCAMY AND E. STEPHAN, *J. Math. Anal. Appl.* **101**, 348 (1984).
3. G. KRIEGSMANN AND C. S. MORAWETZ, *J. Comput. Phys.* **28**, 181 (1978).
4. G. KRIEGSMANN AND C. S. MORAWETZ, *SIAM J. Sci. Stat. Comput.* **1**, 371 (1980).
5. K. S. YEE, *IEEE Trans. AP-S* **14**, 302 (1966).
6. A. TAFLOVE AND K. R. UMASHANKAR, *IEEE Trans. AP-S* **30**, 617 (1982).
7. G. MUR, *IEEE Trans. Electromagn. Compat.* **23**, 377 (1981).
8. K. R. UMASHANKAR AND A. TAFLOVE, *IEEE Trans. Electromagn. Compat.* **24**, 397 (1982).
9. A. TAFLOVE AND K. R. UMASHANKAR, *IEEE Trans. Electromagn. Compat.* **25**, 433 (1983).
10. B. ENGQUIST AND A. MAJDA, *Math. Comp.* **31**, 629 (1977).
11. R. W. P. KING AND S. PRASAD, *Fundamental Electormagnetic Theory and Applications* (Prentice-Hall, Englewood Cliffs, NJ., 1986), p. 154.

12. M. E. LEE, S. I. HARIHARAN, AND N. IDA, NASA Technical Memorandum 100875, ICOMP-88-10, June 1988 (unpublished).
13. R. C. MACCAMY AND M. SURI, *Q. Appl. Math.* **44**, 675 (1987).
14. F. G. FRIEDLANDER, in *Proc. Roy. Soc. London Ser. A* **269**, 53 (1962).
15. A. BAYLISS AND E. TURKEL, *Comm. Pure Appl. Math.* **23**, 707 (1980).
16. C. H. WILCOX, *Comm. Pure Appl. Math.* **9**, 115 (1956).
17. W. L. WEEKS, *Electromagnetic Theory for Engineering Applications* (Wiley, New York, 1964), p. 516.
18. B. ENGQUIST AND A. MAJDA, *Comm. Pure Appl. Math.* **32**, 313 (1979).
19. S. I. HARIHARAN AND S. I. SUDHARSANAN, *J. Sci. Comput.* **2**, 371 (1987).
20. A. C. CANGELLARIS, C. C. LIN, AND K. K. MEI, *IEEE Trans. AP-S* **35**, 1160 (1987).
21. G. E. FORSYTHE AND W. R. WASOW, *Finite Difference Methods for Partial Differential Equations* (Wiley, New York, 1960), p. 444.